Benchmarking Interfacial Magnetic Interactions and Spin Hall Angle in Heavy Metal /CoFeB/MgO Heterostructures

Royston J. J. Lim[1†], T.S. Suraj[2†], Anuj Kumar[2], Jifei Huang[2], Hang Khume Tan[1], Nelson C. B. Lim[1], Pin Ho[1], Shaohai Chen[1]*, Anjan Soumyanarayanan[1,2]*

[1] *Institute of Materials Research & Engineering, Agency for Science, Technology & Research (A*STAR), Singapore 138634*

[2] *Department of Physics, National University of Singapore, Singapore 117551*

† denotes equal author contributions
** denotes corresponding authors*

Abstract

The stability and efficient electrical control of chiral spin textures (CST) is critical for their implementation in racetrack device architectures. Three principal properties determine the utility of material platforms for spin-texture dynamics: perpendicular magnetic anisotropy (PMA), Dzyaloshinskii-Moriya interaction (DMI), and spin Hall angle (SHA). Notwithstanding individual studies, a comprehensive benchmarking of these key interactions across racetrack-compatible material systems remains lacking. Here, we systematically evaluate tunnel-readout compatible HM/CoFeB/MgO trilayers fabricated using wafer-scale techniques. Their key properties – PMA, DMI, and SHA – were characterized across four heavy metals (Pt, W, Ta, Ir) and two CoFeB compositions using magnetometry, spectroscopy, and transport techniques respectively. Our results reveal that W-based stacks exhibit robust PMA and high SHA, while Pt-based stacks provide the strongest DMI. Notably, both DMI and SHA depend strongly on both heavy metal and CoFeB composition, underscoring the critical role of alloy engineering in controlling interfacial magnetic properties. Our work provides quantitative benchmarks and materials design principles for developing next-generation CST-based racetrack devices.

A. Introduction

1. Chiral spin textures (CSTs) such as domain walls and skyrmions are nanoscale spin configurations with considerable potential for advanced spintronic applications.[1, 2] A leading example is racetrack memory, which uses CSTs as bits to encode information along magnetic tracks.[3] Foundational efforts have achieved deterministic, current-driven domain wall manipulation in magnetic heterostructures, establishing the potential for racetrack-based memory and logic devices.[4, 5] Recent developments have extended these to skyrmions, and demonstrated spatially resolved motion at high-speeds – enhancing their potential bit density and operational efficiency.[6, 7] Meanwhile, practical implementations of such racetrack devices require robust CST stability, efficient electrical manipulation and switching, and accurate readout.

2. Deterministic electrical readout and manipulation of CSTs is critical for integrating racetrack memory into practical technologies. Efficient readout can be achieved via magnetic tunnel junctions (MTJs), wherein tunnel magnetoresistance (TMR) affords high signal-to-noise ratio (~200%), with inherent CMOS compatibility.[8] A typical MTJ comprises a magnetic free layer (FL), an insulating tunnel barrier, and a magnetic reference layer (RL). Integration of crystalline MgO barrier with a ferromagnet (FM) such as CoFeB yields robust, large TMR values.[8] Concurrently, spin–orbit torque (SOT) has emerged as an energy-efficient method for CST manipulation, significantly boosting device functionality and efficiency.[9, 10]

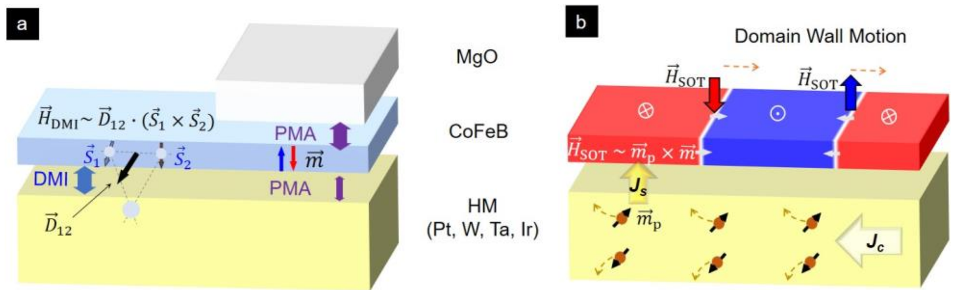

Figure 1. Schematic of (a) interfacial DMI (D) and PMA interactions – key to stabilizing chiral spin textures, and (b) interfacial SOT, used to move Néel-type domain walls in HM/CoFeB/MgO stack. The SHA of the HM governs the threshold charge current density (J_c) need to drive the domain wall.

3. The critical magnetic parameters governing CST formation and manipulation are – perpendicular magnetic anisotropy (PMA), interfacial Dzyaloshinskii–Moriya interaction (DMI), and spin Hall angle (SHA) (Fig 1). PMA determines the tendency for perpendicular magnetization alignment – essential for CST stabilization.[11] Meanwhile, both DMI and SHA originate from inversion symmetry breaking at heavy metal (HM)/FM interfaces.[12, 13] DMI enforces CSTs with fixed Néel chirality, enabling predictable current-induced motion,[14] while SHA, the charge-to-spin conversion efficiency, determines the efficacy of their motion.[15] PMA and DMI collectively govern the stability and geometry of CSTs,[16, 17] thereby influencing racetrack device characteristics.[18]

4. Several previous efforts have individually characterized PMA, DMI, and effective SHA in HM/CoFeB/MgO heterostructures. First, high PMA is typically achieved by either boron-absorbing HMs (e.g. Ta and W) that enhance Fe-O and Co-O interactions at the CoFeB/MgO interface,[19-21] or by specific HMs (e.g. Pt, Ir) via interfacial interactions at the HM/CoFeB interface.[22-24] Next, high DMI values are typically reported at HM interfaces with elemental FMs, such as Pt/Co, and Ir/Fe.[25, 26] Finally, SHA strongly depends on the choice of HM. While Pt, W, Ta etc. are commonly employed due to their large SHA, enabling strong SOTs, [27-29] effective SHA also depends on interfacial spin transparency.[30] Despite numerous efforts, studies have predominantly addressed individual properties or specific material combinations, which vary across reports and systems. A comparative analysis of all critical properties across HMs and CoFeB compositions – crucial for identifying racetrack-compatible stack platforms – remains to be performed.

5. Here, we systematically examine PMA, DMI, and SHA in HM/CoFeB/MgO trilayers, exploring different HMs (Pt, W, Ta, Ir) and CoFeB alloy compositions. Our principal findings include: (a) consistent PMA across nearly all systems post-annealing, pronounced in Ir- and W-based stacks; (b) sizable DMI in Pt-based stacks; and (c) effective SHA in W-based stack configurations. We also observe systematic differences in properties with varying CoFeB composition. Collectively, our results identify W- and Pt-based stacks as possessing optimized interfacial properties for efficient SOT-mediated CST control.

B. Methods

6. The multilayer stacks developed in this work consist of Ta (0 or 3)/HM (5 or 6)/CoFeB (0.7–1.4)/MgO (1.8)/Pt (3) layers (thickness in nm in parentheses). The stacks were deposited on 200 mm Si/SiO_2 wafers by ultra-high vacuum magnetron sputtering at room temperature. Here, Pt, W, Ta, and Ir were selected as HMs to span a range of boron-gettering abilities and spin–orbit coupling strengths. Meanwhile, $Co_{60}Fe_{20}B_{20}$ (CFB_{622}) and $Co_{20}Fe_{60}B_{20}$ (CFB_{262}) compositions were used to assess the impact of CoFeB alloy variations. Using a wedged deposition technique, approximately 60 samples of varying CoFeB thicknesses ("HM/CFB_{622}" and "HM/CFB_{262}") were fabricated. Following deposition, all wafers were post-annealed at 300 °C for 60 min to emulate standard MTJ processing conditions.[31] For characterization, thin film samples with varying thicknesses were prepared for anisotropy and DMI measurements, and associated Hall-bars (60 μm × 10 μm) device samples were fabricated for transport characterization of SHA.

C. Results

Magnetization and Anisotropy

7. Bulk magnetic CoFeB naturally favors in-plane (IP) easy axis. Interfacial engineering is crucial to induce PMA in HM/CoFeB/MgO heterostructures. Key mechanisms include hybridization between Co/Fe (3*d*) and O (2*p*) orbitals at the CoFeB/MgO interface,[19] Co/Fe (3*d*) - HM (5*d*) orbital interactions at the HM/CoFeB interface,[23, 24] and the formation of interfacial high PMA alloys (e.g. CoPt, FePt) during post-deposition annealing.[32, 33] In this context, boron-gettering HMs combined with annealing can enhance PMA by promoting interfacial crystallinity.[19, 34] However, annealing can also lead to interfacial intermixing, creating magnetic dead layers that reduce the effective ferromagnetic volume. This complicates accurate evaluation of magnetic properties. To enable reliable comparisons across stack compositions, the dead layer thickness (t_d) was first extracted from linear fits of saturation magnetization (M_S) as a function of CoFeB thickness (t_{CFB}) for each stack, where t_d corresponds to the x-intercept (Fig. 2a, b). The M_S was obtained from hysteresis loops (Supporting Information S1).

8. The extracted t_d values, summarized in Fig. 2c and Table I, reveal a pronounced dependence on the HM layer, with minimal sensitivity to CoFeB composition. W/CoFeB and Ir/CoFeB stacks have moderate t_d (~0.3 nm), attributed primarily to the CoFeB/MgO interface.[35] Meanwhile, Ta/CoFeB stacks have much larger t_d (~0.44–0.54 nm), consistent with enhanced interfacial intermixing.[36] Finally, Pt/CoFeB stacks exhibit the smallest t_d, with Pt/CFB_{622} presenting slightly negative values, likely due to proximity-induced magnetization.[37] These analyses were used to correct the effective CoFeB thickness (t_{eff} = t_{CFB} - t_d), and extract the effective saturation magnetization ($M_{S,eff}$). Overall, we see in Fig. 2d and Table I that HM/CFB_{622} stacks have $M_{S,eff} \approx 1.28$ MA/m, lower than that for HM/CFB_{262} (~1.55 MA/m). This is in agreement with the expected trends for Co-rich c.f. Fe-rich CoFe alloys.[38] Here, W-based stacks exhibit reduced composition sensitivity, while Pt-, Ta-, and Ir-based stacks display stronger dependence on CoFeB alloying. This is likely due to differences in interfacial bonding and boron redistribution during annealing.

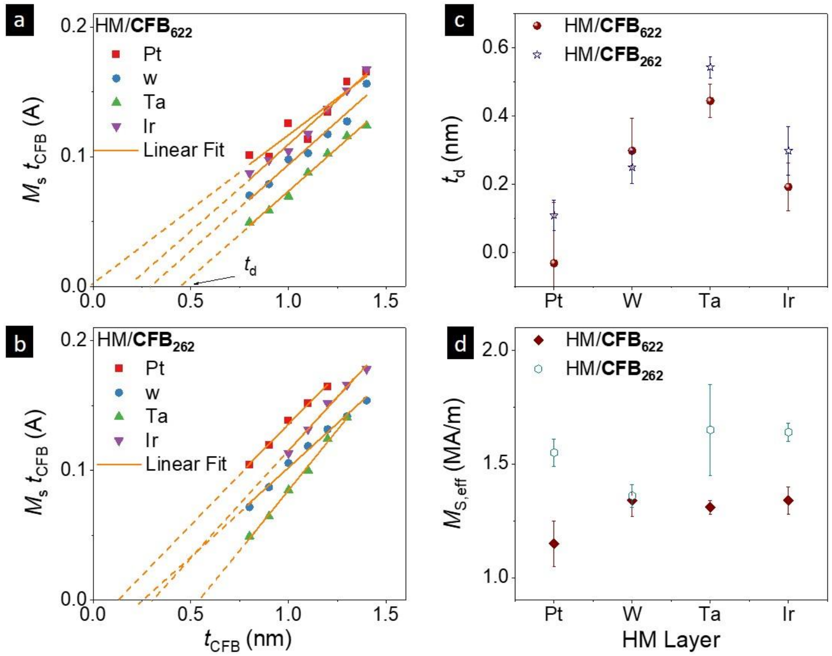

Figure 2 (a, b) Plots of $M_s t_{CFB}$ against FM thickness t_{CFB} for (a) HM/CFB_{622} and (b) HM /CFB_{262} stacks (HM = Pt, W, Ta, Ir). The dead layer thickness (t_d) is estimated as the x-intercept of the linear fit to each curve. (c, d) The variation of thus extracted t_d (c) and effective magnetization $M_{s,eff}$ (d) across the HM/CoFeB stacks (details in text).

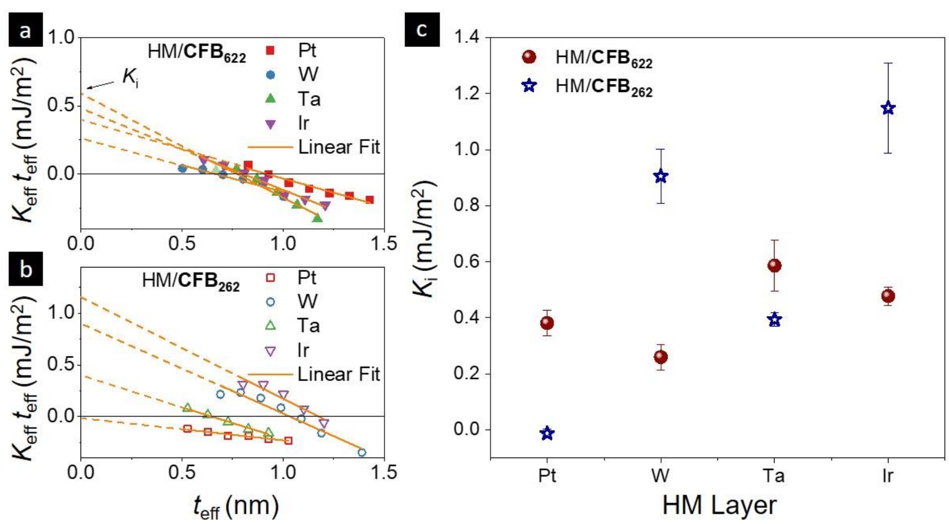

Figure 3 (a, b) Plots of $K_{eff}\, t_{eff}$ against effective FM thickness t_{eff} (= t_{CFB} - t_d) for (a) HM/$\mathbf{CFB_{622}}$ and (b) HM/$\mathbf{CFB_{262}}$ stacks. The interfacial anisotropy, K_i is estimated as the y-intercept of the linear fit to each curve. (c) The variation of extracted K_i across HM/CFB stacks.

9. For ultrathin films, where interfacial effects dominate, the effective anisotropy, K_{eff}, is typically expressed as[31, 39]:

$$K_{eff} \cdot t_{eff} = K_i + (K_u - 2\pi M_{S,eff}^2) \cdot t_{eff} \quad (1),$$

where K_i, K_u and $2\pi M_{S,eff}^2$ denote the interfacial, magnetocrystalline, and shape anisotropies, respectively. To determine K_i – the parameter of interest – K_{eff} was first obtained from the areal difference between IP and out-of-plane (OP) hysteresis loops (Supporting Information S2). Linear fits of $K_{\mathrm{eff}} \cdot t_{\mathrm{eff}}$ versus t_{eff} yield K_{i} as the y-intercept (Fig. 3a, b). The extracted values are summarized in Fig. 3c and Table I.

Table I. Measured magnetic properties for HM/CFB stacks with varying composition – dead layer thickness (t_{d}), effective CoFeB magnetization ($M_{\mathrm{S,eff}}$), interfacial magnetic anisotropy (K_i) and interfacial DMI (D_{int}). See text for details on measurements and analyses.

HM	CoFeB Composition	t_{d} (nm)	$M_{\mathrm{s,eff}}$ (MA/m)	K_{i} (mJ/m^2)	D_{int} (pJ/m)
Pt	20:60:20	0.11±0.04	1.55±0.06	-0.01±0.02	**0.92±0.07**
	60:20:20	-0.03±0.17	1.15±0.10	0.38±0.05	**1.53±0.06**
W	20:60:20	0.25±0.04	1.36±0.05	**0.90±0.09**	0.10±0.01
	60:20:20	0.30±0.09	1.34±0.07	0.26±0.05	0.31±0.02
Ta	20:60:20	0.54±0.03	1.65±0.20	0.39±0.02	-0.05±0.03
	60:20:20	0.44±0.05	1.31±0.03	**0.59±0.09**	0.11±0.02
Ir	20:60:20	0.30±0.07	1.64±0.04	**1.15±0.16**	0.12±0.05
	60:20:20	0.19±0.07	1.34±0.06	0.48±0.03	-0.23±0.06

10. The K_i values are positive for nearly all stacks, and exhibit systematic trends with varying HM type and CoFeB composition. Overall, the HM/CFB_{622} stacks exhibit lower K_i variation (0.26-0.59 mJ/m^2) than the HM/CFB_{262} stacks (-0.013-1.15 mJ/m^2). For Pt-based stacks, Pt/CFB_{262} (Pt/CFB_{622}) have small negative (positive) K_i, consistent with prior reports. These may be attributed to Fe–O bond disruption[40] and Pt–Co orbital hybridization[24, 32], respectively. Next, both Ta-based stacks show comparable K_{i}, likely due to cooperative contributions from both interfaces.[41] Meanwhile, for both W and Ir, the CFB_{262} stacks demonstrate significantly enhanced K_{i} - 2~3 times higher than their CFB_{622} counterparts. This is likely driven by W's boron-gettering effect and enhanced Fe–O bonding,[19, 34] and by Ir–Fe hybridization at the HM/CoFeB interface[23], respectively.

Interfacial DMI

11. DMI plays a crucial role in stabilizing CSTs by introducing a fixed sense of magnetization rotation (chirality) to the spin structure. In this work, DMI was quantified using wave vector-resolved BLS spectroscopy across HM and CoFeB compositions. Compared to domain wall expansion methods, BLS provides a parameter-free robust approach for quantifying DMI[42-44]. Figures 4a-b show the schematics of the measurement setup and spectra, respectively. For finite DMI, BLS spectra exhibit nonreciprocal frequency shifts (Δf) between the Stokes (S) and anti-Stokes (AS) resonance peaks, which can be determined by Lorentzian fitting. This asymmetric Δf, measured for opposite wave vectors (k) by applying an external magnetic field H_{ext} along ±x-direction, follows the relation[45, 46]:

$$f(k)_{asym} = \frac{f(-k)-f(k)}{2} = \frac{\gamma D k}{\pi M_{\mathrm{s,eff}}} \quad (2)$$

where γ is the gyromagnetic ratio (176 GHz/T), and D is the micromagnetic DMI. For a representative dataset (Pt/CFB_{622} stack: Fig. 4c), BLS analysis yielded an averaged DMI of 0.8 ± 0.06 mJ/m² (Supporting Information S3).

12. To facilitate direct comparison of DMI across stacks of different thicknesses, the interfacial DMI parameter ($D_{\mathrm{int}} = D \times t_{\mathrm{CFB}}$) was calculated for all HM/CoFeB stacks. The data summarized in Fig. 4d and Table I show that all stacks exhibit positive D_{int}, except Ta/CFB_{262} and Ir/CFB_{622}. Comparing the magnitude ($|D_{\mathrm{int}}|$), HM/CFB_{622} stacks display higher values relative to HM/CFB_{262} stacks. Furthermore,

$|D_{int}|$ follows a clear trend across HMs: Pt >> W ≈ Ir > Ta. Notably, for a nominal CoFeB thickness of 1 nm, the Pt/CFB_{622} stack delivers the highest DMI, reaching 1.53 mJ/m².

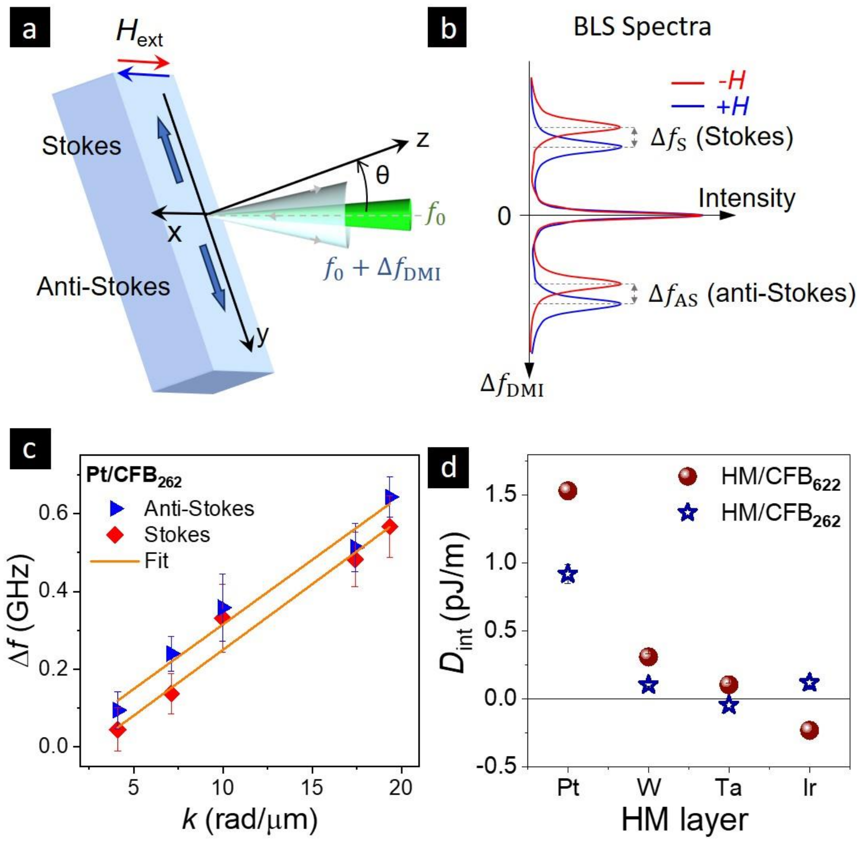

Figure 4 (a) Schematic representation of the BLS measurement geometry, and magnon scattering processes relevant to DMI measurements. (b) Schematic BLS spectra illustrating shifts in Stokes and anti-Stokes magnon peaks for magnetic fields (H_{ext}) applied along ±x (blue, red) directions. (c) Dispersion of frequency difference (Δf) with wavevector (k), and corresponding linear fits for the Pt/CFB_{622} stack. (d) Resulting variation of interfacial DMI (slope of linear fit in (c)), D_{int}, across the HM/CoFeB stacks in this work.

13. The variation of interfacial DMI with HMs and CFB composition can be understood as arising from electronic structure variations due to spin-orbit coupling (SOC) and broken symmetry effects[47]. For HM(W[48], Ta[49])/CFB_{262} stacks, positive DMI has been reported in the literature, consistent with our results. Conversely, negative DMI has been reported for Ir/Co[26], in line with our Ir/CFB_{622} stacks. Compositional gradients within CoPt alloys have been shown to influence the DMI sign.[50] Additionally, prior studies indicate that Ir/Co and Pt/Co interfaces share the same DMI sign[26, 51], while Ir/Fe and Pt/Co interfaces exhibit opposite signs.[16] These trends result from SOC and electronic structure at HM/FM interfaces, due to interfacial hybridization and broken inversion symmetry.[47] Thus, the negative D_{int} for Ta/CFB_{262} is attributed to interfacial alloy formation, while the positive D_{int} for Ir/CFB_{262} likely arises from the Ir/Fe interface.

Spin Hall Angle

14. In SOT-based HM/FM devices, the SHA θ_{SH} quantifies the efficiency of spin–charge conversion. A larger θ_{SH} enables more efficient SOT generation, reducing the critical current for magnetization switching or CST manipulation. To quantify θ_{SH}, both spin-torque ferromagnetic resonance (ST-FMR) and harmonic Hall measurement techniques are widely employed.[52, 53] ST-FMR utilizes the microwave response of FMs, and is typically limited to FMs with IP easy axis. In contrast, harmonic Hall measurements employ a simple, versatile four-probe lock-in technique – compatible with both IP- and PMA samples, and capable of resolving damping-like (H_{DL}) and field-like (H_{FL}) torque components. Figure 5a shows the device geometry used for harmonic Hall measurements in this work (Supporting Information S4). Following device fabrication, anomalous Hall measurements were first performed to confirm PMA (Fig. 5b). Next, first- ($V_{1\omega}$) and second-harmonic ($V_{2\omega}$) Hall voltages were measured under applied IP magnetic fields. SOT-induced longitudinal/transverse ($H_{L/T}$) fields and the $H_{DL(FL)}$ were determined using

$$H_{\mathrm{L(T)}}|_{J_e} = \left(\frac{\partial V_{2\omega}}{\partial H} / \frac{\partial^2 V_{1\omega}}{\partial H^2}\right)_{x(y)} \quad (3)$$

and $$H_{\mathrm{DL(FL)}}|_{J_e} = -2\,\frac{H_{\mathrm{L(T)}} \pm 2\varepsilon H_{\mathrm{T(L)}}}{1-4\varepsilon^2} \quad (4),$$

respectively, where ε is the ratio of planar to anomalous Hall voltages (Supporting Information S5).

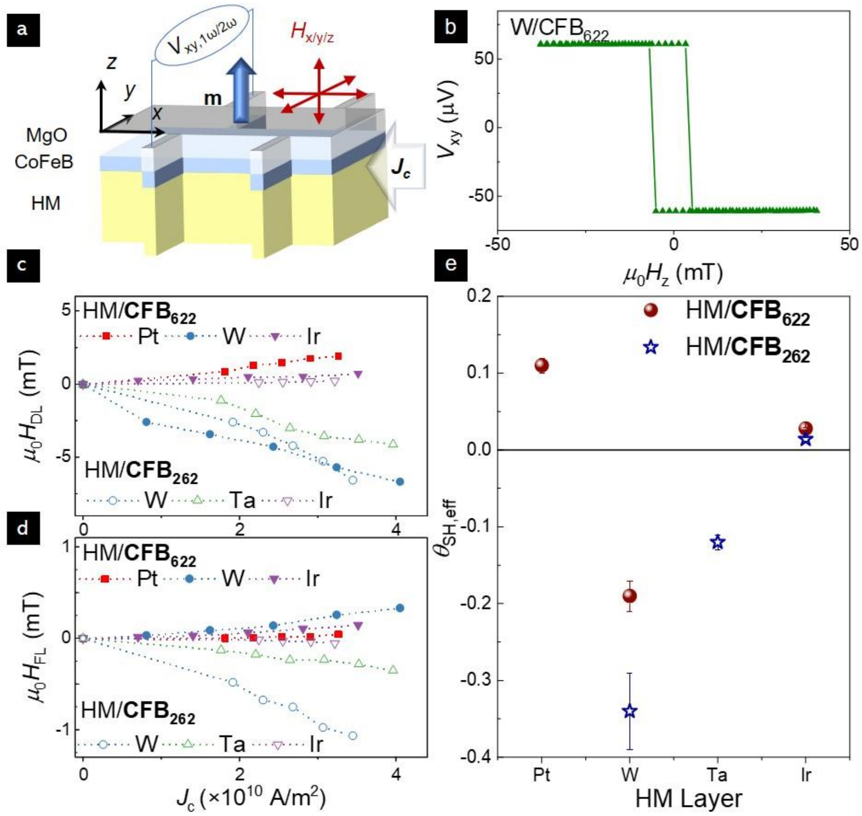

Figure 5 (a) Schematic of the harmonic Hall response measurement of HM/CFB Hall bar devices. A charge current J_c is applied along +x, with external magnetic field $H_{x/y/z}$ (subscript indicates axis). The first and second harmonic Hall signals ($V_{1\omega/2\omega}$) were obtained simultaneously. (b) Measured AHE, $V_{xy}(H_z)$ for the W/CFB$_{622}$ stack, with $J_c = 2.7 \times 10^{10}$ A/m^2. (c-e) Variation of SOT induced effective fields for (c) damping-like ($\mu_0 H_{DL}$) and (d) field-like ($\mu_0 H_{FL}$) torques for J_C over 0 - 4 × 10^{10} A/m^2. (e) The resulting variation of effective SHA $\theta_{SH,eff}$ across HM/CFB stacks.

15. Figures 5c (5d) summarize the extracted $H_{DL(FL)}$ with varying current density J_e. The slope of these curves represents the corresponding torque efficiency, $\beta_{DL(FL)}$. The effective SHA ($\theta_{SH,eff}$) was thus calculated using:

$$\theta_{\mathrm{SH,eff}} = \frac{4eM_{s,\mathrm{eff}}t_{\mathrm{CoFeB}}}{\pi\,\hbar}\beta_{\mathrm{DL}}, \quad (5)$$

as summarized in Fig. 5e and Table II. The W/CFB$_{622}$ stack exhibits the highest ε value, due to a strong planar Hall contribution. Likewise, W/CFB stacks also show the largest $|\beta_{DL/FL}|$ and $|\theta_{SH,eff}|$ values,

Table II. Measured key harmonic Hall transport properties for HM/CFB stacks with varying composition – ratio of planar to anomalous Hall voltages signals (ε), damping-like (β_{DL}) and field-like (β_{FL}) torque coefficients, and effective spin Hall angle ($\theta_{SH,eff}$).

HM	CoFeB Composition	ε (%)	β_{DL} (10^{-11} mT·A^{-1}·m^2)	β_{FL} (10^{-11} mT·A^{-1}·m^2)	$\theta_{SH,eff}$
Pt	60:20:20	5.8±0.7	6.2±0.4	-0.5±0.1	**0.11±0.01**
W	20:60:20	26.0±1.7	-23.7±3.7	5.8±2.0	**-0.34±0.05**
	60:20:20	71.7±0.2	-14.9±1.6	20.3±1.9	**-0.19±0.02**
Ta	20:60:20	6.9±0.8	-10.8±0.8	-0.9±0.1	**-0.12±0.01**
Ir	20:60:20	4.6±0.3	0.7±0.1	-0.1±0.04	0.014±0.002
	60:20:20	2.1±0.4	1.8±0.2	0.6±0.1	0.028±0.002

underscoring the efficient SOT generation for W.[54] Across stacks, positive $\theta_{SH,eff}$ values were observed for Pt/CFB and Ir/CFB, and negative values for W/CFB and Ta/CFB. In terms of $|\theta_{SH,eff}|$ magnitude, the trend is: W > Ta ≈ Pt >> Ir. Finally, the W/CFB$_{262}$ (-0.34) displayed a higher $|\theta_{SH,eff}|$ than the W/CFB$_{622}$ (-0.19).

16. Previous studies have shown that the magnitude and sign of $\theta_{SH,eff}$ are primarily determined by the HM layer. Reported values vary widely with HM thickness and fabrication conditions – for Pt (0.07–0.12)[13, 27], W (–0.08 – –0.64)[29, 55, 56], Ta (–0.1 – –0.35) [13, 28, 56], and Ir (0.02–0.04)[42, 49]. Consistent with the overall trends, this work benchmarks the HM variation of $\theta_{SH,eff}$ under identical deposition conditions. For W and Ta, $|\theta_{SH,eff}|$ is sensitive to the crystalline phase – with higher magnitudes for the β-phase (W: 0.64[29], Ta: 0.35[28]) than the α-phase (W: 0.08[55], Ta: 0.16[56]). For our case (t_{HM} ~5-6 nm, annealed at 300 °C), the data suggests that W layers may have mixed α/β-phase composition, whereas Ta is predominantly in the α-phase. Finally, a notable observation is the sizable discrepancy of $\theta_{SH,eff}$ between W/CFB$_{622}$ (-0.19) and W/CFB$_{262}$ (-0.34), as there are no prior reports of

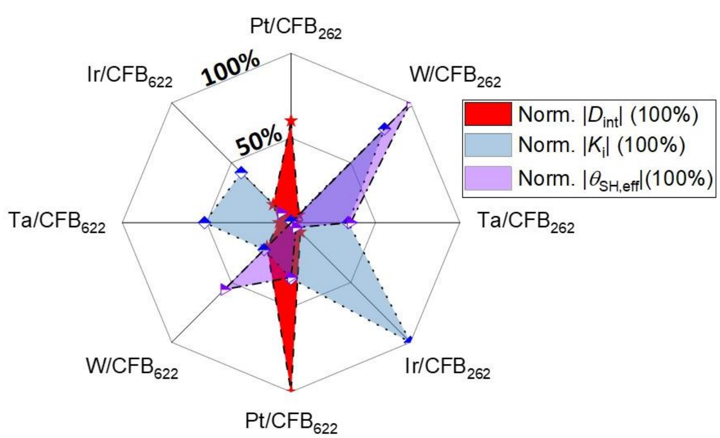

Figure 6 Radar plots of normalized magnitudes of key magnetic parameters - $|D_{int}|$ (red), $|K_i|$ (teal) and $|\theta_{SH,eff}|$ (magenta) across the HM/CoFeB stacks. The plotted values are normalized to the corresponding maximum values (see Tables I and II).

CoFeB composition-induced changes in SHA. We speculate that the enhanced $|\theta_{SH,eff}|$ in W/CFB$_{262}$ could arise from altered interfacial bonding or spin transparency, which warrants further investigation in future works.

D. Discussion and Conclusion

17. We have performed a comprehensive evaluation of HM-FM heterostructures identified as promising for MTJ-compatible racetrack devices. Across 8 such HM/CFB/MgO trilayer stacks, we have benchmarked the interfacial anisotropy K_i, DMI (D_{int}), and effective SHA ($\theta_{SH,eff}$). To enable intuitive comparison, $|K_i|$, $|D_{int}|$, and $|\theta_{SH,eff}|$, normalized to their respective maxima (across all stacks), are presented as a radar plot (Fig. 6). The comparison shows that W/CFB and Pt/CFB_{622} offer complementary strengths as all-electrical CST platforms: high SHA and anisotropy for W, and robust DMI for Pt. Beyond performance benchmarking, our systematic screening study also uncovers valuable findings on the sensitivity of both DMI and $\theta_{SH,eff}$ to CoFeB composition and HM combinations – well beyond the scope of individual material studies.

18. While no single stack configuration can fully address all three requirements, promising candidates could be optimized to enhance their utility for racetrack devices. For W-based stacks, alloying with additional HMs (e.g., W_xIr_{100-x} [57]) could complement the intrinsically large SHA and PMA with sizable DMI – thereby augmenting both skyrmion stability and SOT efficiency. For Pt-based stacks, improved boron-gettering strategies can strengthen interface crystallinity[22, 23], improving interfacial anisotropy and TMR. Moreover, finely-tuned annealing protocols offer an additional lever to modulate material properties[20, 39], enabling optimization for specific device designs and application requirements.

19. In addition to standalone HM/FM/MgO free layers, our stacks can also be effectively implemented as building blocks within composite free layer architectures for CSTs. In such structures, a chiral underlayer (HM1/FM/HM2) establishes spin texture stability and supports SOT manipulation, while the top layer is optimized for TMR readout and SOT. [58] For such applications, W-based stacks emerge as the natural choice for the top layer due to their high PMA and TMR. Our results elucidate their recently shown efficacy for CST readout, via either interlayer exchange coupling (IEC) or dipolar coupling, or a combination of both mechanisms.[59-61] Our findings on the influence of CoFeB composition on SHA and PMA provide valuable insights for optimizing the properties of both components in composite stack structures.

Acknowledgements. We acknowledge helpful discussions with Jing Zhou, and experimental inputs from Idayu Lim, Joshua Cheong and Bee Chun Lim. This work was supported by A*STAR (grant nos. A18A6b0057: SpOT-LITE, and M23M6c0112: ChiRes), NUS (grant no. A-0004544-00-00), and the Singapore Ministry of Education Academic Research Fund (Tier-1 grant no. 23-1072-A0001).

AUTHOR DECLARATIONS

Conflict of Interest

All the authors have no conflicts of interest to disclose.

DATA AVAILABILITY

The data that support the findings of this study are available within the article.

References

1. Fert, A., N. Reyren, and V. Cros, *Magnetic skyrmions: advances in physics and potential applications.* Nature Reviews Materials, 2017. **2**(7): p. 17031.
2. Yang, S.-H., et al., *Chiral spintronics.* Nature Reviews Physics, 2021. **3**(5): p. 328-343.
3. Parkin, S.S.P., M. Hayashi, and L. Thomas, *Magnetic Domain-Wall Racetrack Memory.* Science, 2008. **320**(5873): p. 190-194.
4. Fukami, S., et al., *A spin-orbit torque switching scheme with collinear magnetic easy axis and current configuration.* Nature Nanotechnology, 2016. **11**(7): p. 621-5.
5. Luo, Z., et al., *Current-driven magnetic domain-wall logic.* Nature, 2020. **579**(7798): p. 214-218.
6. Jeon, J.-C., et al., *Multicore memristor from electrically readable nanoscopic racetracks.* Science, 2024. **386**(6719): p. 315-322.
7. Pham, V.T., et al., *Fast current-induced skyrmion motion in synthetic antiferromagnets.* Science, 2024. **384**(6693): p. 307-312.
8. Djayaprawira, D.D., et al., *230% room-temperature magnetoresistance in CoFeB ∕ MgO ∕ CoFeB magnetic tunnel junctions.* Applied Physics Letters, 2005. **86**(9).
9. Miron, I.M., et al., *Perpendicular switching of a single ferromagnetic layer induced by in-plane current injection.* Nature, 2011. **476**(7359): p. 189-193.
10. Manchon, A., et al., *Current-induced spin-orbit torques in ferromagnetic and antiferromagnetic systems.* Reviews of Modern Physics, 2019. **91**(3): p. 035004.
11. Soumyanarayanan, A., et al., *Emergent phenomena induced by spin–orbit coupling at surfaces and interfaces.* Nature, 2016. **539**(7630): p. 509-517.
12. Crépieux, A. and C. Lacroix, *Dzyaloshinsky–Moriya interactions induced by symmetry breaking at a surface*. Journal of Magnetism and Magnetic Materials, 1998. **182**(3): p. 341-349.
13. Liu, L., et al., *Spin-Torque Switching with the Giant Spin Hall Effect of Tantalum.* Science, 2012. **336**(6081): p. 555-558.
14. Thiaville, A., et al., *Dynamics of Dzyaloshinskii domain walls in ultrathin magnetic films.* Europhysics Letters, 2012. **100**(5): p. 57002.
15. Emori, S., et al., *Current-driven dynamics of chiral ferromagnetic domain walls.* Nat Mater, 2013. **12**(7): p. 611-6.
16. Soumyanarayanan, A., et al., *Tunable room-temperature magnetic skyrmions in Ir/Fe/Co/Pt multilayers.* Nature Materials, 2017. **16**(9): p. 898-904.
17. Je, S.-G., et al., *Asymmetric magnetic domain-wall motion by the Dzyaloshinskii-Moriya interaction.* Physical Review B, 2013. **88**(21): p. 214401.
18. Parkin, S. and S.-H. Yang, *Memory on the racetrack.* Nature Nanotechnology, 2015. **10**(3): p. 195-198.
19. Yang, H., et al., *First-principles investigation of the very large perpendicular magnetic anisotropy at Fe| MgO and Co| MgO interfaces.* Physical Review B, 2011. **84**(5): p. 054401.
20. Mukherjee, S., et al., *Role of boron diffusion in CoFeB/MgO magnetic tunnel junctions.* Physical Review B, 2015. **91**(8): p. 085311.
21. Sinha, J., et al., *Influence of boron diffusion on the perpendicular magnetic anisotropy in Ta|CoFeB|MgO ultrathin films.* Journal of Applied Physics, 2015. **117**(4).
22. Peng, S., et al., *Giant interfacial perpendicular magnetic anisotropy in MgO/CoFe/capping layer structures.* Applied Physics Letters, 2017. **110**(7).
23. Odkhuu, D., et al., *Extremely large perpendicular magnetic anisotropy of an Fe(001) surface capped by 5d transition metal monolayers: A density functional study.* Physical Review B, 2013. **88**(18): p. 184405.
24. Nakajima, N., et al., *Perpendicular Magnetic Anisotropy Caused by Interfacial Hybridization via Enhanced Orbital Moment in Co/Pt Multilayers: Magnetic Circular X-Ray Dichroism Study.* Physical Review Letters, 1998. **81**(23): p. 5229-5232.
25. Soucaille, R., et al., *Probing the Dzyaloshinskii-Moriya interaction in CoFeB ultrathin films using domain wall creep and Brillouin light spectroscopy.* Physical Review B, 2016. **94**(10): p. 104431.
26. Ma, X., et al., *Interfacial Dzyaloshinskii-Moriya Interaction: Effect of5d Band Filling and Correlation with Spin Mixing Conductance.* Physical Review Letters, 2018. **120**(15): p. 157204.

27. Nguyen, M.-H., et al., *Enhanced spin Hall torque efficiency in Pt100−xAlx and Pt100−xHfx alloys arising from the intrinsic spin Hall effect.* Applied Physics Letters, 2016. **108**(24).
28. Sagasta, E., et al., *Unveiling the mechanisms of the spin Hall effect in Ta.* Physical Review B, 2018. **98**(6): p. 060410.
29. Chen, W., et al., *Temperature study of the giant spin Hall effect in the bulk limit of β-W.* Physical Review B, 2018. **98**(13): p. 134411.
30. Zhang, W., et al., *Role of transparency of platinum–ferromagnet interfaces in determining the intrinsic magnitude of the spin Hall effect.* Nature Physics, 2015. **11**(6): p. 496-502.
31. Ikeda, S., et al., *A perpendicular-anisotropy CoFeB-MgO magnetic tunnel junction.* Nature Materials, 2010. **9**(9): p. 721-4.
32. Caminale, M., et al., *Spin pumping damping and magnetic proximity effect in Pd and Pt spin-sink layers.* Physical Review B, 2016. **94**(1): p. 014414.
33. Chen, S., et al., *Structure, magnetic and thermal properties of FePt–C–BN granular films for heat assisted magnetic recording.* Journal of Physics D: Applied Physics, 2020. **53**(13): p. 135002.
34. Pai, C.-F., et al., *Enhancement of perpendicular magnetic anisotropy and transmission of spin-Hall-effect-induced spin currents by a Hf spacer layer in W/Hf/CoFeB/MgO layer structures.* Applied Physics Letters, 2014. **104**(8).
35. Pandey, C.A., et al., *Enhancing perpendicular magnetic anisotropy through dead layer reduction utilizing precise control of Mg insertions.* Journal of Magnetism and Magnetic Materials, 2020. **511**: p. 166956.
36. Kim, S., et al., *Contributions of Co and Fe orbitals to perpendicular magnetic anisotropy of MgO/CoFeB bilayers with Ta, W, IrMn, and Ti underlayers.* Applied Physics Express, 2017. **10**(7): p. 073006.
37. Tan, H.K., et al., *Intermixing induced anisotropy variations in CoB-based chiral multilayer films.* Journal of Physics D: Applied Physics, 2021. **54**(35): p. 354003.
38. Rizal, C., et al., *Magnetic properties of nanostructured Fe-Co alloys.* Journal of Applied Physics, 2013. **113**(11).
39. Chen, S., et al., *Ferromagnetic alloy material CoFeC with high thermal tolerance in MgO/CoFeC/Pt structure and comparable intrinsic damping factor with CoFeB.* Journal of Physics D: Applied Physics, 2018. **51**(5): p. 055006.
40. Du, W., et al., *Stack structure and CoFeB composition dependence of perpendicular magnetic anisotropy employing Pt heavy metal layer.* Journal of Alloys and Compounds, 2022. **928**: p. 167205.
41. Wang, Y., et al., *First-principles study of origin of perpendicular magnetic anisotropy in MgO|CoFeB|Ta structures.* Results in Physics, 2023. **45**: p. 106239.
42. Böttcher, T., et al., *Quantifying symmetric exchange in ultrathin ferromagnetic films with chirality.* Physical Review B, 2023. **107**(9): p. 094405.
43. Kuepferling, M., et al., *Measuring interfacial Dzyaloshinskii-Moriya interaction in ultrathin magnetic films.* Reviews of Modern Physics, 2023. **95**(1): p. 015003.
44. Kim, D.-Y., et al., *Quantitative accordance of Dzyaloshinskii-Moriya interaction between domain-wall and spin-wave dynamics.* Physical Review B, 2019. **100**(22): p. 224419.
45. Di, K., et al., *Direct Observation of the Dzyaloshinskii-Moriya Interaction in a Pt/Co/Ni Film.* Physical Review Letters, 2015. **114**(4): p. 047201.
46. Nembach, H.T., et al., *Linear relation between Heisenberg exchange and interfacial Dzyaloshinskii–Moriya interaction in metal films.* Nature Physics, 2015. **11**(10): p. 825-829.
47. Zhu, L., et al., *Critical role of orbital hybridization in the Dzyaloshinskii-Moriya interaction of magnetic interfaces.* Communications Physics, 2022. **5**(1): p. 151.
48. Jaiswal, S., et al., *Investigation of the Dzyaloshinskii-Moriya interaction and room temperature skyrmions in W/CoFeB/MgO thin films and microwires.* Applied Physics Letters, 2017. **111**(2).
49. Lo Conte, R., et al., *Role of B diffusion in the interfacial Dzyaloshinskii-Moriya interaction in $Ta/Co_{20}Fe_{60}B_{20}/MgO$ nanowires.* Physical Review B, 2015. **91**(1): p. 014433.
50. Zhang, Q., et al., *Quantifying the Dzyaloshinskii-Moriya Interaction Induced by the Bulk Magnetic Asymmetry.* Physical Review Letters, 2022. **128**(16): p. 167202.
51. Ishikuro, Y., et al., *Dzyaloshinskii-Moriya interaction and spin-orbit torque at the Ir/Co interface.* Physical Review B, 2019. **99**(13): p. 134421.

52. Chen, S., et al., *Giant spin torque efficiency in single-crystalline antiferromagnet Mn2Au films.* Science China Materials, 2021. **64**: p. 2029-2036.
53. Nguyen, M.-H. and C.-F. Pai, *Spin–orbit torque characterization in a nutshell.* APL Materials, 2021. **9**(3).
54. Cho, S. and B.-G. Park, *Large planar Hall effect in perpendicularly magnetized W/CoFeB/MgO structures.* Current Applied Physics, 2015. **15**(8): p. 902-905.
55. Pai, C.-F., et al., *Spin transfer torque devices utilizing the giant spin Hall effect of tungsten.* Applied Physics Letters, 2012. **101**(12).
56. Qian, L., et al., *Spin Hall effect in the α and β phases of* Ta_xW_{1-x} *alloys.* Physical Review B, 2020. **102**(9): p. 094438.
57. Luo, X., et al., *Modulation of Spin-Orbit Torque and Large Enhancement of Perpendicular Magnetic Anisotropy in* $W/Co_{20}Fe_{60}B_{20}/MgO$ *by Ir Insertion Layer.* Physical Review Applied, 2023. **19**(3): p. 034043.
58. Toh, A.K.-J., et al., *Evolution of zero-field skyrmionic states in exchange-coupled composite multilayer nanodots.* Physical Review Applied, 2024. **22**(2): p. 024036.
59. Guang, Y., et al., *Electrical Detection of Magnetic Skyrmions in a Magnetic Tunnel Junction.* Advanced Electronic Materials, 2023. **9**(1): p. 2200570.
60. Chen, S., et al., *All-electrical skyrmionic magnetic tunnel junction.* Nature, 2024. **627**(8004): p. 522-527.
61. Urrestarazu Larrañaga, J., et al., *Electrical Detection and Nucleation of a Magnetic Skyrmion in a Magnetic Tunnel Junction Observed via Operando Magnetic Microscopy.* Nano Letters, 2024. **24**(12): p. 3557-3565.